Article

Optoelectronic structure and photocatalytic applications of Na(Bi,La)S solid solutions with tunable bandgaps

Amal BaQais, Nina Tymi#ska, Tangui Le Bahers, and Kazuhiro Takanabe

Chem. Mater., **Just Accepted Manuscript** • DOI: 10.1021/acs.chemmater.9b00031 • Publication Date (Web): 03 Apr 2019

Optoelectronic structure and photocatalytic applications of $Na(Bi,La)S_2$ solid solutions with tunable bandgaps

Amal BaQais[a,b] , Nina Tymińska[c], Tangui Le Bahers*[c], Kazuhiro Takanabe *[a,d]

[a]King Abdullah University of Science and Technology (KAUST), KAUST Catalysis Center (KCC) and Physical Sciences and Engineering Division (PSE), 4700 KAUST, Thuwal 23955-6900, Saudi Arabia.

[b]Department of Chemistry, College of Sciences, Princess Nourah bint Abdulrahman University (PNU), Riyadh 11671, Saudi Arabia.

[c]Univ Lyon, ENS de Lyon, CNRS, Université Claude Bernard Lyon 1, Laboratoire de Chimie UMR 5182, F-69342 Lyon, France.

[d]Department of Chemical System Engineering, School of Engineering, The University of Tokyo, 7-3-1 Hongo, Bunkyo-ku, Tokyo 113-8656, Japan.

ABSTRACT: $NaLa_{1-x}Bi_xS_2$ solid solutions with tunable bandgaps were synthesized, and their optoelectronic structures and photocatalytic performance were investigated via experimental and theoretical approaches. The solid-solution powders with various La/Bi ratios were synthesized with Na_2CO_3, La_2O_3 and Bi_2O_3 as precursors and via sulfurization with flowing CS_2 at 800 °C for 2 h. The Vegard's law behavior of cell parameters showed a perfect Bi/La solid solution in the cubic $NaLa_{1-x}Bi_xS_2$ with the associated linear variation of the lattice constants. On the contrary, the combination of diffuse reflectance UV−Vis spectroscopy with density functional theory (DFT) calculations employing the HSE06 functional reveals a monotonic but non-linear variation of the bandgap of the solid solution. While consistent valence band maximum (VBM) was obtained in $NaLa_{1-x}Bi_xS_2$—consisting mainly of S 3p orbitals—the conduction band minimum (CBM) was contributed by discrete Bi orbitals present at more positive potential than La. As a result, the slight inclusion of Bi caused a drastic shift in the bandgap, and 24% Bi substitution provided an absorption edge closer to that of pure $NaBiS_2$. Systematic DFT calculations on $NaLa_{1-x}Bi_xS_2$ determined the optoelectronic properties for improved photovoltaic and photocatalytic performance with a Bi-rich sample rather than a La-rich counterpart; i.e., there were larger absorption coefficients, smaller effective masses, and larger dielectric constants for Bi-rich samples versus La-rich samples. The $NaLa_{1-x}Bi_xS_2$ particles decorated with Pt nanoparticles show maximum hydrogen evolution performance with x = 0.02-0.06 of Bi samples consistent with the compensating effects between photon absorption capacity and loss of electromotive force with decreasing bandgap.

INTRODUCTION

Energy harvested from solar irradiation needs appropriate storage in the form of transportable chemicals or fuels. Heterogeneous photocatalysts are generally based on a semiconductor in a powder form ideally absorbing a substantial portion of the sunlight and generally decorated with electrocatalysts on its surface to achieve surface redox reactions that generate chemicals in a single reactor.[1-3] Several semiconductor families have been developed for visible light absorption including (oxy)nitrides, (oxy)sulfides, and oxyfluorides for photocatalytic water splitting;[4-7] however their photocatalytic efficiency remains lower than the desired photoconversion efficiency for practical applications.[8-9] Therefore, designing efficient and cost-effective photocatalysts is a key research area especially for large-scale applications.

The $AgBiS_2$ semiconductor has a bandgap below 1.2 eV and high absorption coefficients in the visible light region for highly efficient solar cell applications.[10] In this context, alkali bismuth ternary sulfides, $ABiS_2$ (A = Li, Na and K), have not been explored to investigate their semiconductor properties although they are environmentally friendly and cost effective versus Ag-based counterparts.[11] Experiments showed that $ABiS_2$ (A = Li, Na and K) crystallize as compounds with a disordered NaCl-type cubic structure,[11] and the primary results of $NaBiS_2$ showed an optical bandgap of ~1.2 eV.[12] This bandgap falls within the ideal range for photovoltaic solar cell requirements or tandem cells.[8, 13] However, this bandgap is often too small for photocatalytic water splitting. The cation or anion substitutions are common approaches for bandgap engineering. Achieving total or partial substitution of the elements while maintaining similar crystal structures alters the conduction band (CB) or valence band (VB) structure. This in turn offers a red or blue shift of the absorption edge.[14-17] In one excellent example, experiment and theory were combined to evaluate the substitution of La in the Bi site in BiCuO(S,Se,Te). This resulted in widening of the optical bandgap from the near-IR to the UV region.[18-23]

The trivalent Bi^{3+} cation has an ionic radius of 117.0 pm similar to the rare earth La^{3+} cation (117.2 pm). The electronegativity values are also similar to facilitate complete substitution of La^{3+} in Bi^{3+} sites. $NaLnS_2$ materials (Ln: La^{3+}, Nd^{3+}, Gd^{3+} and Lu^{3+}) have two crystal structures according to the crystal radius ratio of Na/Ln. The compound crystallizes in a cubic NaCl type structure (space group $Fm\bar{3}m$) when the ratio is smaller than 1.033.[24-26] Beyond this value, the compounds form hexagonal α-$NaFeO_2$ (space group $R\bar{3}m$).[24, 27] According to Isaacs et al. and Li et al., $NaLaS_2$ was successfully synthesized, but its optical properties have not yet been reported.[28-29]

This work uses a design concept that is extended from oxysulfides to the sulfide materials. The possibility of a Bi/La solid solution on the same sublattice is expected to retain the crystal lattice symmetry of the original materials due to the similar ionic radii and valency of the two cations. A judicious chemical substitution would lead to band engineering—this could modulate charge separation, diffusion, and transport properties to meet the requirements of photocatalytic water splitting.

To date, $NaBiS_2$ powder material is obtained via a hydrothermal route[12]; it was recently synthesized via a solution phase method.[30] The difficulty of using these protocols for $NaLaS_2$ synthesis is associated with the strong affinity of La for oxygen (water), which leads to the formation of unavoidable lanthanum oxide impurities. To avoid this obstacle, a dry sulfurization process was applied here including flowing dry CS_2 as a sulfur source over oxides/carbonates powder precursors. Thus, a single-phase solid solution of $NaLa_{1-x}Bi_xS_2$ was successfully synthesized reflecting the original precursor ratio. We report here how the stoichiometric substitution of La with Bi affects the optoelectronic properties along with photocatalytic performance of $NaLa_{1-x}Bi_xS_2$ by joining the experimental and theoretical characterization steps.[31]

METHODOLOGY

Synthesis of $NaLa_{1-x}Bi_xS_2$. $NaLa_{1-x}Bi_xS_2$ materials were synthesized via the preparation method proposed by Masuda et al.[24] Lanthanum oxide (La_2O_3, Aldrich 99.99%) and/or bismuth oxide (Bi_2O_3, Aldrich 99.99%) and sodium carbonate ($NaCO_3$, Aldrich, anhydrous, 99.99%) were the starting metal precursors of La, Bi, Na. Carbon disulfide (CS_2, Aldrich, anhydrous ≥99%) was used as the sulfurization agent. For the optimization, 3 mmol La_2O_3 or Bi_2O_3 was thoroughly ground with 3.3 mmol Na_2CO_3 in an agate mortar for 10 min. For the solid solution, the synthesis was performed by varying the bismuth percentage in the final product to be 2, 6, 12, 24, 50 and 75% (Table S1). The mixture was placed on an alumina boat and inserted into the alumina reaction tube of a horizontal electric furnace. The sulfurization process was conducted by flowing a saturated vapor of CS_2 (40 kPa) in N_2 at a flow rate of 50 ml min^{-1} (Figure S1 shows the schematic diagram of the setup). The furnace temperature was subsequently raised at 20 K min^{-1} to 800 °C and maintained there for 2 h. CS_2 gas was introduced to the reaction when the tube temperature reached 500 °C. After the reaction, the furnace was cooled to room temperature. The resulting solid powder was collected and washed with water and ethanol several times and then dried at 60 °C. The mass yield of the recovered powder was calculated based on the La or Bi content.

X-ray diffraction (XRD). The crystal structure of the resulting samples were characterized at room temperature using Bruker D8 Advanced A25 diffractometer equipped with a Cu X-ray tube (Cu–Kα; λ = 0.154 nm) operating at 40 kV and 40 mA in the Bragg–Brentano geometry using a linear position-sensitive detector with an opening of 2.9°. The diffractometer was configured with a 0.44° divergence slit, a 2.9° anti-scatter slit, and 2.5° Soller slits. A nickel filter was used to attenuate contributions from Cu–Kβ radiation. Data sets were acquired over the 2θ range of 10–80°, and the integration step size of 0.019° resulted in a counting time of 50 s per step. The crystallite sizes were determined by applying the Debye–Scherrer equation. Rietveld analysis used the Fullprof program (v6.00).[32]

Inductively coupled plasma optical emission spectrometry (ICP-OES). The stoichiometric molar ratios of $NaLa_{1-x}Bi_xS_2$ were determined by ICP-OES using a Varian 720-ES. Before the analysis, a known amount of the material was digested by microwave in 5 mL of concentrated nitric acid 70% using 1000 W power at 220 °C for 20 min (ETHOS 1 from Milestone). The solution was subsequently diluted with Milli-Q water to a 200 mL total volume before ICP-OES analysis.

Scanning electron microscopy (SEM) and energy-dispersive X-ray spectroscopy (EDX). The size and morphology of the particles were studied by field emission SEM at 5 keV on a Nova Nano 630 instrument from FEI. The powders were directly pressed onto the SEM stub. The chemical compositions were investigated with a X-ray energy dispersive spectroscopy (EDX) EDAX's APOLLO XL EDS detector with 30 mm^2 SDD sensor equipped on Nova NanoSEM630 (Thermo Fisher Scientific) operating at 23 kV.

Transmission electron microscopy (TEM). Bright-field (BF)-TEM, selected area electron diffraction (SAED), and X-ray Energy Dispersive Spectroscopy (EDS) measurements used a Titan 80–300 CT TEM equipped with a field emission gun at an accelerating voltage of 300 kV. Prior to the analysis, the samples were dispersed in acetone followed by sonication of 10 min by using bath sonication. A drop of the solution was poured onto a copper-grid supporting a holey carbon film. The grid was dried in air prior to TEM observations. Microscope settings and magnification range were selected such as the morphology as well as high-resolution (HR) TEM information can be obtained. The interplanar d-spacing were obtained both from the SAED patterns and the Fast-Fourier Transform (FFT) of the HRTEM micrographs. Elemental mapping used a post-column energy filter of model GIF Tridiem 863 from Gatan, Inc. The entire TEM analysis was performed using the Gatan Microscopy Suite (GMS v. 1.83) software package from Gatan, Inc.

Ultraviolet−Visible (UV−Vis) spectroscopy. Diffuse reflectance spectra (DRS) were collected using a JASCO model V-670 spectrophotometer equipped with a diffuse reflectance accessory. The spectra were recorded from 300 to 1100 nm using halogen and deuterium lamps as the light sources. The reflectance spectra can be

represented using the Kubelka–Munk (KM) function $f(R) = (\alpha/S) = (1 - R)^2 / 2R$ where α is the absorption coefficient, S is the scattering coefficient, and R is the diffuse reflectance at a given photon energy. The absorption band edges were estimated from the analysis of spectra as described in the main manuscript.

X-ray photoelectron spectroscopy (XPS). XPS studies were done on a Kratos Axis Ultra DLD spectrometer equipped with a monochromatic Al Ka X-ray source ($h\nu$ = 1486.6 eV) operating at 150 W as well as a multi-channel plate and delay line detector under a ~9-10 mbar vacuum. All spectra were recorded using an aperture slot of 300 μm × 700 μm. Survey spectra were collected using a pass energy of 160 eV and a step size of 1 eV. A pass energy of 20 eV and a step size of 0.1 eV were used for the high-resolution spectra. For XPS analysis, the samples were mounted in floating mode to avoid differential charging. Binding energies were referenced to the C 1s peak at 284.8 eV.

Ultraviolet Photoelectron Spectroscopy (UPS). UPS was performed were carried out in the same XPS instrument using a He I excitation ($h\nu$ = 21.21 eV). A bias of −9 V was applied to the sample surface for UPS measurements. The UPS measurements were performed to determine the changing in the work function with Bi substitutions. The work function is defined as the energy necessary to remove an electron from the Fermi level of a semiconductor infinitely far away, i.e., to vacuum level. This gave the cutoff of secondary electrons in the UPS spectra.[33] Eq. 1 was used to calculate the work functions of the films:

$$\Phi = h\nu - E_{\text{cutoff}} \quad (1)$$

where Φ, $h\nu$ (21.21 eV), and E_{cutoff} are work function, incoming photon energy from He I source, and the secondary electron cutoff energy, i.e., width of the spectra, respectively.

Photoelectron emission spectroscopy in air (PESA). The VB positions were determined by using a Riken Keiki AC-2 photoelectron spectrometer. FTO glass (2 cm × 1 cm) was used as the substrate. These were cleaned well with sonication in acetone and then ethanol for 10 min followed by N_2 gas drying at room temperature before the coating. Using a DC power supply (PowerPac™ Universal Power Supply), the electrophoretic deposition method was employed to immobilize 100 mg of powder dispersed in 100 ml of a mixture of acetone with 10 mg of iodine after sonication for 10 min. A constant voltage at 60 V was applied between two FTO plates for about 3 min. The substrate was then removed from the suspension and dried in an oven at 60 °C for 1 h. The standard hydrogen potential was calculated relative to the absolute vacuum potential.[34]

$$E_{abs} = E_{SHE} + 4.44\ V \quad (2)$$

Photocatalytic Reaction. The photocatalytic reaction was conducted in a recirculating batch reactor connected to a gas chromatography (GC) unit equipped with a vacuum line.[35] The reactant solution was maintained at room temperature using a flow of cooling water during the reaction. Photocatalyst powder (100 mg) was dispersed in 100 mL of 0.2 M Na_2S and 0.5 M Na_2SO_3 with 52 μL of 0.1 M H_2PtCl_6. $6H_2O$ solutions (1 wt % Pt equivalent) and then sonicated for 15 min in an ultrasonic bath. This Pt solution was used as a source of the Pt cocatalyst that was photodeposited under irradiation during the reaction. Before irradiation, the reaction vessel was degassed several times to remove dissolved air followed by the introduction of 13 kPa of Ar gas into the photocatalytic system. A Xe lamp (CERMAX PE300-BF, 300 W) was used as a light source, and the irradiation wavelength was controlled with a combination of a cold mirror and a water filter ((λ > 350 nm); the photon distribution is shown in Figure S2). The homogeneity of the solution during the reaction was maintained via magnetic stirring. Samples of the evolved gases were extracted periodically and analyzed with a GC (Bruker 450 GC, TCD, Ar gas, molecular sieve 13X). Action spectra, i.e., the apparent quantum efficiencies (AQE) as a function of wavelengths, were measured using bandpass filters (Tokina). XRD analysis after the stability test was performed by collecting the powder that was washed by water and ethanol and then dried at 60°C overnight.

Computational Details. We first performed geometry optimizations and frequency calculations under the Density Functional Theory framework using the hybrid PBE0[36] functional as implemented in the *ab initio* CRYSTAL17 code.[37] Next, we used HSE06[38] single-point calculations on the PBE0 optimized structures to obtain details on the electronic properties,[39] which is also done with this code. Finally, the transport properties were estimated from the effective masses and mobilities of the charge carriers. This final property was computed within the Boltzmann transport theory (BTE) framework involving a constant scattering time (τ) and the rigid band approximation[40-42] using CRYSTAL17 code. In addition, the optical properties[43] were obtained from the single-point calculations at the HSE06 level of theory using VASP code (version 5.3.5).[38,44-46] For the solid solutions, we focused on the lowest energy (i.e., thermodynamically most stable) configurations unless specified otherwise. Figure S3 illustrates the scheme of $NaLa_{1-x}Bi_xS_2$ structures. Details on the computed method were added to the Supporting Information.

RESULTS AND DISCUSSION

Synthesis and Structural Characterizations.

Solid solutions of $NaLa_{1-x}Bi_xS_2$ were prepared by varying their precursor ratios (Table S1). The synthesis was performed under these optimized conditions: 10% excess Na_2CO_3, flow rate of 50 ml min^{-1}, and 800 °C for 2 h. The detailed optimization of the synthesis protocol is described in the Supporting Information (Figure S4, Table S2). The observed X-ray diffraction of $NaLaS_2$ and $NaBiS_2$ patterns coincide well with the calculated patterns from the literature (PDF 00-038-1391) and (PDF 00-008-0406) for pure $NaLaS_2$ and $NaBiS_2$, respectively, (Figure 1). $NaLaS_2$ and $NaBiS_2$ materials have a cubic NaCl-type structure where the sulfur occupies the chlorine sublattice, while cations (Na and La/Bi) statistically occupy the Na sublattice as a solid solution.[12, 27, 47] The final mass yields were ~86% and ~90% based on lanthanum and bismuth, respectively. the single-phases of $NaLa_{1-x}Bi_xS_2$ solid solutions were obtained by varying the molar ratio of Bi to La; there was no impurity phase.

The substitution of Bi in the La site was confirmed by shifting of the 2θ toward higher angles (see Figure 1).

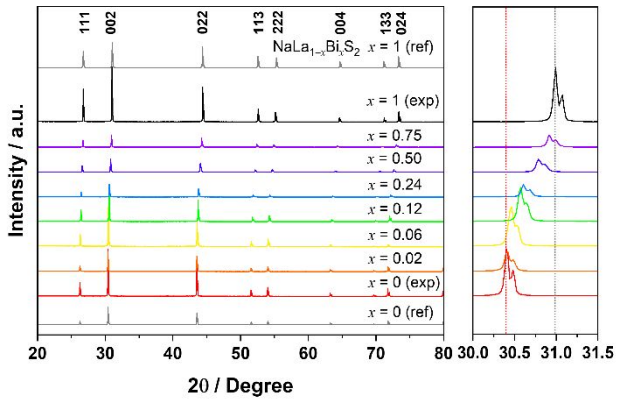

Figure 1. XRD patterns of $NaLa_{1-x}Bi_xS_2$ with an enlarged view for the 002 peak on the right.

The XRD patterns of the $NaLa_{1-x}Bi_xS_2$ materials were refined using the Rietveld method (Figure S5). The unit cell lattice constants determined by these refinements are presented in Table S3 and also show the corresponding values obtained by DFT calculations with the PBE0 functional. The average discrepancy between experiment and DFT is around 0.3% for $NaLaS_2$ and 0.6% for $NaBiS_2$; these values were below the 1.2% standard deviation of the PBE0 functional.[39] A linear shift of the obtained lattice parameters by the La/Bi ratios is explained by Vegard's relationship (Eq. 3) suggesting that homogeneous solid solutions were formed over the entire composition range rather than a physical mixture of the segregated $NaLaS_2$ and $NaBiS_2$ phases. A small lattice mismatch of ~1.95 % based on Eq. 4 was obtained resulting in strong cation-cation interactions and completely miscible Bi and La in the cationic site.[48,49]

$$a_{La_{(1-x)}Bi_x} = (1-x)a_{La} + xa_{Bi} \quad (3)$$

$$\text{Lattice mismatch degree } \% = \frac{a_{La} - a_{Bi}}{a_{Bi}} \times 100 \quad (4)$$

Going from $NaLaS_2$ to $NaBiS_2$, the lattice constant and the cell volume consistently decreased in agreement with the slight difference in ionic radii between La^{3+} (117.2 pm) and Bi^{3+} (117.0 pm). The chemical compositions of the solid solution were confirmed using ICP-OES analysis (Table 1). The ICP-OES results agreed with the nominal compositions. Therefore, we continued using sample notation based on the precursor ratios.

Table 1. Targeted stoichiometry and the measured composition in of $NaLa_{1-x}Bi_xS_2$ using ICP analysis.

Targeted stoichiometry $NaLa_{1-x}Bi_xS_2$	Stoichiometric molar ratio determined by ICP		
x =	Bi/(La+Bi)	Na/(La+Bi)	S/(La+Bi)
0	0	1	1.94
0.02	0.02	0.99	1.95
0.06	0.06	1.02	2
0.12	0.13	0.98	2
0.24	0.24	1	1.90
0.50	0.52	1	1.99
0.75	0.74	1	2.05
1	1	1.06	2.04

Morphology and surface characterization.

The morphology of the products was observed with SEM. The random particles in the micrometer size range for all $NaLa_{1-x}Bi_xS_2$ solid solutions are shown in Figure S6. Going from $NaLaS_2$ to $NaBiS_2$ material, the particle size increased possibly due to bismuth sulfide being a flux agent facilitating particle size growth. This finding is consistent with the melting point trend where the Bi sample has a lower value than the La sample (e.g., Bi_2S_3; 760-850 °C, vs. La_2S_3; 2100-2150 °C).[50]

The microstructures of the $NaLa_{1-x}Bi_xS_2$ solid solutions were further investigated using HRTEM, and the images are presented in Figure 2. The HRTEM images for all the $NaLa_{1-x}Bi_xS_2$ solid solution exhibit high crystallinity of single-phase compounds. The selected area electron diffraction (SAED) patterns and the corresponding fast Fourier transform (FFT) of the $NaLa_{1-x}Bi_xS_2$ show distinct bright spots indicating that the particles are single crystal phase. All index zones agreed well with the XRD results (Figure 1). For example, the inter-planar distance between the fringes of 2.07 Å and 2.04 Å are consistent with the (022) crystal plane of $NaLaS_2$ and $NaBiS_2$, respectively, and the spacings of the lattice of 2.93 Å, 2.93 Å, and 2.91 Å are consistent with the spacings of the corresponding (002) planes for $NaLa_{0.98}Bi_{0.02}S_2$, $NaLa_{0.88}Bi_{0.12}S_2$, and $NaLa_{0.50}Bi_{0.50}S_2$, respectively. The inter-planar distance between the fringes of the $NaLa_{0.94}Bi_{0.06}S_2$ FFT image matches the d-spacing of (111) plane. An ultrathin amorphous layer of ~2 nm was detected on the surface of all samples most likely due to the unavoidable oxidation of the surface upon the exposure to air as discussed in XPS analysis below.

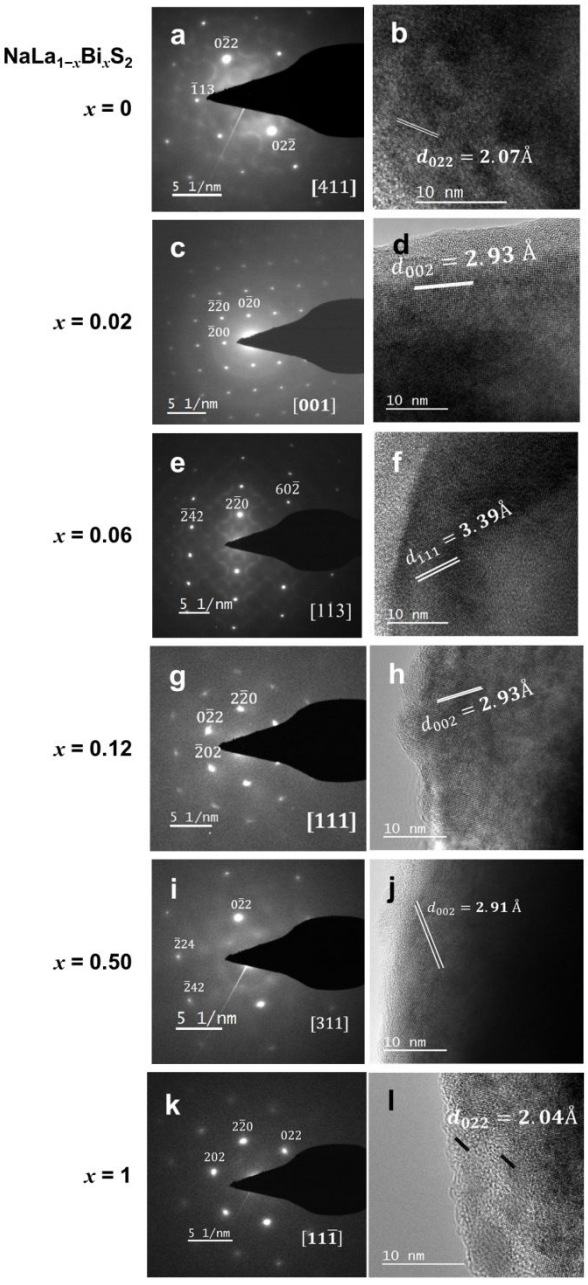

Figure 2. Selected area electron diffraction patterns (left row) and high-resolution TEM images (right row) of (a, b) $NaLaS_2$, (c, d) $NaLa_{0.98}Bi_{0.02}S_2$, (e, f) $NaLa_{0.94}Bi_{0.06}S_2$, (g, h) $NaLa_{0.88}Bi_{0.12}S_2$, (i, j) $NaLa_{0.50}Bi_{0.50}S_2$, and (k, l) $NaBiS_2$.

Elemental mapping with TEM/EDX is shown in Figure S7. La, Bi, and S are well-distributed throughout the microspheres indicating the formation of a homogeneous solid solution. The lack of Na is most likely due to easy reduction and vaporization of Na via the 300 kV electron beam as described for alkali metals.[30] The ICP and EDX (23 kV) results confirmed the stoichiometric ratios of solid solutions (Table 1 and Table S5).

XPS analysis was used to investigate the surface composition and its oxidation state. A wide survey spectra and high-resolution spectra of $NaLaS_2$, $NaLa_{0.50}Bi_{0.50}S_2$, and $NaBiS_2$ are shown in Figure S8a. The binding energy of the Na 1s core level was located at 1071.46 eV (Figure S8b). This value matches nicely with Na in the commercial sodium sulfides and sodium polysulfides indicating that Na existed in a monovalent state for all solid solution compositions.[30,51] The spectra of S 2s in Figure S8c shows that there are two species of S present in the materials. Most have a binding energy of approximately 224.70 eV (metal sulfides) with a trace amount likely being sulfate species.[51,52] The La 3d states of $NaLaS_2$ and $NaLa_{0.50}Bi_{0.50}S_2$ (Figure S8d) split into doublets peaks for spin orbits of La $3d_{5/2}$ and La $3d_{3/2}$ at binding energies of 834.8-835.1 eV and 851.7-851.8 eV, respectively, suggesting that La^{3+} predominates as reported in La_2S_3.[52]

The peaks on the high energy side of the $3d_{5/2}$ (at 838.4 eV in $NaLaS_2$ and 838.9 eV in $NaLa_{0.50}Bi_{0.50}S_2$) and $3d_{3/2}$ (at 855.3 eV in $NaLaS_2$ and 855.7 eV in $NaLa_{0.50}Bi_{0.50}S_2$) peaks correspond to their shake-up satellites. Peaks were observed at 837 and 853.9 eV (more obvious in $NaLaS_2$). This are due to other oxidized impurities (La-O-S) that could be caused by lanthanum sulfate formation consistent with the S 2s results. $NaBiS_2$ and $NaLa_{0.50}Bi_{0.50}S_2$ materials exhibit Bi $4f_{7/2}$ and Bi $4f_{5/2}$ at 158.2 eV and 163.5 eV, respectively, with peak gaps of 5.3 eV. This confirms the Bi^{3+} trivalent oxidation state (Figure S8e). The weak peak intensity of the oxidized S in $NaBiS_2$ suggests that bismuth is comparatively more resistant to oxidation than the La-containing sample.

Optical absorption characterization and electronic structure.

Diffuse reflectance UV−Vis measurements of the $NaLa_{1-x}Bi_xS_2$ samples were conducted, and their Kubelka-Munk function are presented in Figure 3. For the pure Bi or La samples, the bandgap of $NaLaS_2$ was 3.15 eV in the UV region, whereas that of $NaBiS_2$ was 1.21 eV. The value reported in the literature for $NaBiS_2$ materials is 1.4 eV[12], and 1.37 eV[30] for direct transition and 1.28 eV[11] and 1.07 eV[30] for indirect transition, respectively. Band structures and the densities of states (DOS) of pure $NaLaS_2$ and $NaBiS_2$ were computed using the HSE06 functional (Figure 4). The computed bandgaps were 3.61 eV for $NaLaS_2$ and 1.37 eV $NaBiS_2$, resulting in a large shift in bandgap from UV to Vis-NIR region. Figure 4a shows that $NaLaS_2$ is characterized by an indirect bandgap. Nevertheless, $NaLaS_2$ also has direct transition at slightly higher energy values by 122 meV than the indirect transition. In contrast, $NaBiS_2$ is characterized by a nearly direct bandgap. Such close proximity of direct and indirect bandgaps can be beneficial in materials used for photo(electro)chemical applications because it results in strong optical adsorption near the fundamental edge and relatively long photo-carrier relaxation time.[53] From the DOS, as shown in Figures 4d, the VBM is dominated by S 3*p* states whereas the CBM is mostly composed of La 5*d* for $NaLaS_2$ and Bi 6*p* for $NaBiS_2$. It is clearly observed that the La 5*d* states lie in a higher energy range (3.6 eV vs. Fermi level E_F) than Bi 6*p* states (1.4 eV vs. Fermi level E_F). It is worth mentioning that the unoccupied La 4*f* states in $NaLaS_2$ have a negligible influence on VBM and CBM, and thus did not affect the bandgap.[23, 54] The low energy level of CBM in $NaBiS_2$ mainly consists of 6*p* orbitals, as commonly observed in bismuth and lead compounds with $6s^26p^0$ electron configuration (Pb^{2+}, Bi^{3+}).[7,14] Na orbitals are almost absent from the VB

confirming that this ion has mainly a structural role and almost no direct effect on the electronic structure.

The absorption coefficients of pure $NaLaS_2$ and $NaBiS_2$ materials were also computed (Figure 4c). For $NaLaS_2$, a high absorption coefficient was obtained to be approximately 1×10^5 cm^{-1} in the near UV-range (400 nm down to 300 nm), but it decreased sharply in the visible light region. Despite the indirect bandgap nature of $NaBiS_2$, high absorption coefficients were attained on the order of 10^5 cm^{-1}: This is an order of magnitude higher than a typical value for direct bandgap semiconductors[55] across the entire UV−Vis range. The refractive index and the extinction and the absorption coefficients along the a, b, and c directions are provided in Figure S10.

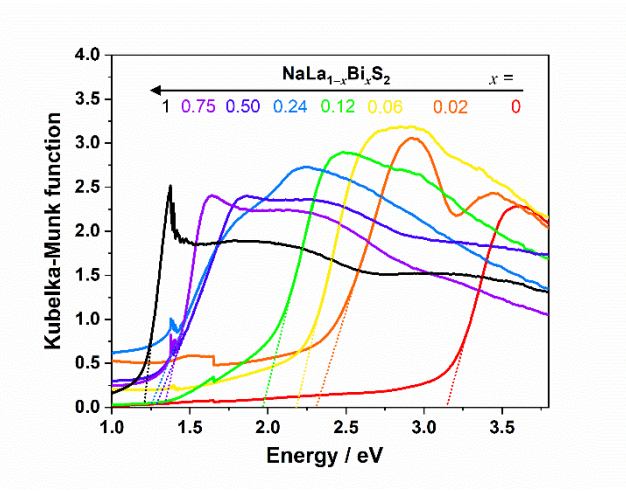

Figure 3. Diffuse reflectance UV-Vis spectra of $NaLa_{1-x}Bi_xS_2$ samples.

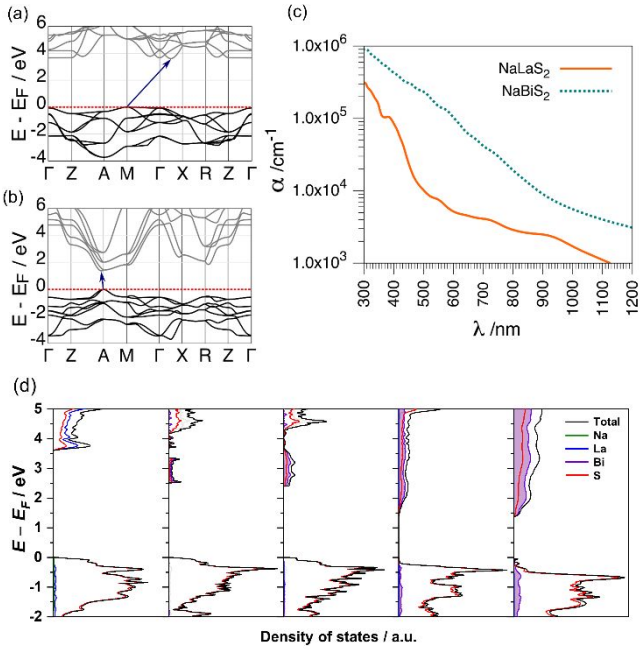

Figure 4. The calculated band structures of (a) $NaLaS_2$ and (b) $NaBiS_2$. (c) The calculated absorption coefficient of $NaLaS_2$ and $NaBiS_2$ as a function of wavelength, and (d) the calculated density of states (DOS) of $NaLa_{1-x}Bi_xS_2$ where x = 0, 0.06, 0.12, 0.50, and 1.

The measured and computed bandgaps of $NaLa_{1-x}Bi_xS_2$ solid solutions are compiled in Figure 5, highlighting the difference in their lattice constants. As discussed for the XRD patterns (Figure 1), the crystal lattice monotonically varied by the composition from $NaLaS_2$ to $NaBiS_2$. In contrast, a small substitution of Bi in $NaLaS_2$ crystal resulted in a drastic reduction of the bandgap after replacing 2%, 6%, and 12% of the Bi in La sites. Substituting 24% Bi onwards led to bandgap close to that of pure $NaBiS_2$. This drastic shift was consistently observed via DFT calculations. Upon Bi substitution, new states located on Bi appear for the CB within the forbidden band of $NaLaS_2$. This drastically reduces the bandgap with a small quantity (see DOS in Figure 4d). At larger Bi concentrations, the band associated with its 6*p* states broadens to reach a width of the CB for pure $NaBiS_2$ at a Bi concentration of 50% (Figure 4d).

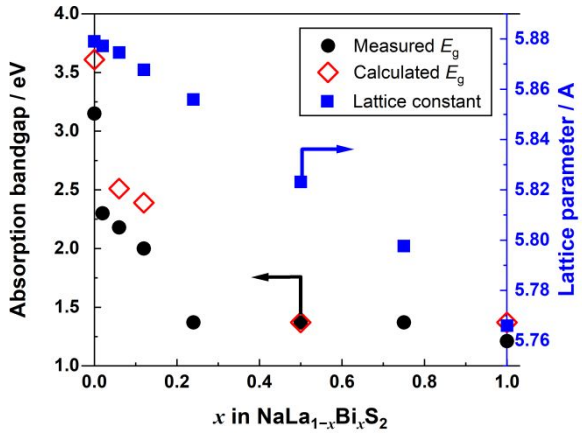

Figure 5. Measured and calculated bandgaps as well as lattice constant as a function of x in $NaLa_{1-x}Bi_xS_2$ composition.

Dielectric and Transport Properties.

After photon absorption, the efficiency of photoconversion relies on a few fundamental steps: exiton dissociation and charge carrier diffusion to the active sites before recombination. These processes depend on the dielectric constant (ε_r), the electron and hole effective masses (m^*), and the exciton binding energies (E_b).[3, 9, 31,39] Table 2 summarizes the calculated optoelectronic properties of $NaBiS_2$ and $NaLaS_2$.

Table 2. Computed optoelectronic properties of pure $NaBiS_2$ and $NaLaS_2$.

Properties	$NaLaS_2$	$NaBiS_2$
E_g (eV)	3.61	1.37
ε_∞	3.81	6.30
ε_r	15.40	20.46
m_e^* [a] (m_e)	0.43	0.27
m_h^* [a] (m_e)	1.63	0.33
m_e*DOS [b] (m_e)	0.07	0.56
m_h*DOS [b] (m_e)	2.95	0.32

μ_e [c] (cm^2 V^{-1} s^{-1})	10-250	1-28
μ_h [c] (cm^2 V^{-1} s^{-1})	1-5	3-55
E_b (meV)	4-42[d]	1-6[d]

[a] Average of [100], [010], [001], [110], [101], and [111] directions. [b] Boltzmann transport theory; provided for carrier density of 1 × 10^{17} cm^{-3}. [c] Estimated under the assumption of τ = 1-10 fs. [d] Using average values of m_e^* and m_h^*.

Starting with dielectric constants, two main factors contribute to the static dielectric constant: (i) the contribution from the electron density (ε_∞) and (ii) the contribution from the ion vibrations (ε_{vib}) as shown in the equation below:

$$\varepsilon_r = \varepsilon_\infty + \varepsilon_{vib} \quad (5)$$

The electronic contribution ε_∞ to the dielectric constant of $NaLaS_2$ is particularly low indicating a poor polarizability of the electron density of this material. In contrast, ε_∞ is much larger for $NaBiS_2$ mainly because the Bi atoms are highly polarizable as observed in other Bi-based oxysulfides such as Bi(Cu,Ag)OS and $Bi_xLa_{1-x}CuOS$.[7, 54,56] This low electronic contribution is partly compensated by a larger contribution coming from vibration, ε_{vib}. The Bi-based material has a larger contribution from vibrations than the La-based one. This larger contribution originates from the larger distortion induced by the Bi-based material versus the ideal NaCl structure allowing more vibrational modes to be involved in the dielectric constant due to the removal of some selection rules.

Because the total dielectric constants of both materials are larger than 10, good exciton dissociation was seen for both materials and were confirmed by the low E_b values calculated in the framework of the Mott-Wannier model.[39] In the case of $NaLaS_2$, the exciton binding energy depends on the model used to compute the effective masses leading to values slightly higher than 25 meV in the worst-case scenario. Overall, in contrast to $NaLaS_2$, $NaBiS_2$ exhibits a larger dielectric constant and lower effective masses of charge carriers. This results in a much lower exciton binding energy. Consequently, a very good efficiency of exciton dissociation can be expected for the Bi-based materials.

The effective masses and charge carrier mobilities were also computed. The effective masses were computed using the parabolic approximation from the band structure and from the DOS-averaged approach from Boltzmann transport theory as implemented in the CRYSTAL17 code. In general, electrons were found to be more mobile than holes in $NaLaS_2$; the opposite was seen for $NaBiS_2$. Albeit, the differences in the effective masses of both charge carriers of the latter material are much smaller than that for $NaLaS_2$. This agrees with the effective masses. The hole mobilities computed from the Boltzmann transport theory (Figure S10) for $NaLaS_2$ are very low (~5 cm^2 V^{-1} s^{-1} when the scattering time (τ) was assumed as 10 fs). For $NaBiS_2$ the μ_h is an order of magnitude higher (c.a. 55 cm^2 V^{-1} s^{-1}). The opposite is true for electron mobility, which is almost 10-fold higher for $NaLaS_2$ than that for $NaBiS_2$. Masuda *et al.* reported the mobility for holes in $NaLaS_2$ to be 20.6 cm^2 V^{-1} s^{-1} at 300 K. This falls into the same order of magnitude computed here.[24] Nevertheless, the order of magnitude of charge carrier mobilities (~10 cm^2 V^{-1} s^{-1}) agrees well with the good charge collection efficiency.

The optoelectronic properties of the $NaLa_{1-x}Bi_xS_2$ solid solutions are given in the Supporting Information. As already discussed, the bandgap varies continuously between those of $NaLaS_2$ and $NaBiS_2$. The electronic contribution to the dielectric constant behaves similarly. Only the vibrational contribution is larger for the solid solution than the native compounds. This is due to the lower symmetry of the solid solution allowing more vibrational modes to contribute to the dielectric constant. The transport properties were not computed because the transport mechanism of the solid solution is probably not based on the rigid band-model but rather on polaronic conductivity due to the localized nature of the CB. The simulation of such type of conductivity involves polaron simulations[31] that go beyond the scope of this work but interested readers should consider the work of Morbec et al.[57]

Band position determination.

The band alignment of CBM and VBM in a semiconductor relative to the redox potentials of the respective photocatalytic reactions is the critical parameter for successful photocatalysis.[58-60] Photoelectron spectroscopy in air measurements (PESA) and UV photoelectron spectroscopy (UPS) were performed to determine the CBM and VBM positions of the synthesized materials. The thin films of solid solution $NaLa_{1-x}Bi_xS_2$ were prepared by electrophoretic deposition method for the powders on fluorine-doped tin oxide (FTO) substrates. Figure S11 shows the XRD patterns of the thin films/FTO; all peaks belong to FTO and to the relative material in a pure phase.

The ionization potentials estimate VBM potentials and were obtained by the crossing point of the linear part of the curve with the background from PESA measurements as presented in Figure S12. The results are summarized in Table S6. The VBM only shifted by 0.25 eV from $NaLaS_2$ to $NaBiS_2$ as expected from the same contribution of S orbitals as discussed previously (Figure 4). Next, the UPS results showed that the measured Fermi level positions of solid solutions drastically decreased by Bi substitution as shown in Figure S13 and Table S6 in agreement with bandgap shift measured from UV−Vis absorption spectra (Figure 3) and the computed DOS (Figure 4). In summary, the scheme representing the band positions of all $NaLa_{1-x}Bi_xS_2$ samples is presented in Figure 6.

The large difference in energy between the Fermi level from UPS data and VB from PESA data is due to Fermi level located close to the CB indicating the n-type character as in the case of other sulfide materials such as CdS and ZnS with sulfur vacancies.[61,62] The CBM of $NaLaS_2$ is more negative than the standard hydrogen potential. The CBMs of 2 and 6% of Bi samples are located at potentials of −0.6 and −0.43 V vs. RHE, respectively, while giving the visible light response. These results agree well with the bandgap narrowing from UV−Vis data and DFT results of these solid solutions. The

CB position of solid solution with 50% Bi content are located at potentials closer to that of pure $NaBiS_2$ material, and they are very close to the standard hydrogen potential.

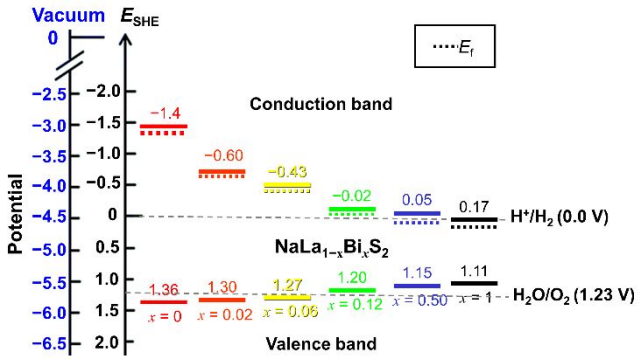

Figure 6. Scheme showing the band positions of VBM and CBM for $NaLa_{1-x}Bi_xS_2$ solid solutions with respect to SHE and vacuum level.

Photocatalytic activity toward H_2 evolution reaction.

The performance of photocatalytic hydrogen generation under UV–Vis light irradiation (photon flux shown in Figure S2) for $NaLa_{1-x}Bi_xS_2$ materials was evaluated (Figure 7a). The Pt particles were loaded by photodeposition during the photocatalytic measurement in the presence of 0.2 M Na_2S and 0.5 M Na_2SO_3 as electron donors. A pure $NaLaS_2$ material immediately generated hydrogen with an initial rate of 2 μmol h^{-1}, and the hydrogen production was stable for over 8 h. Interestingly, substitution of 2 and 6% Bi in the La site shows improved photocatalytic performance, and the photocatalytic rates enhance to 4.4 and 7.1 μmol h^{-1}. This result is consistent with the large overlap between the used photon irradiation and photon absorption (Figure 7b).

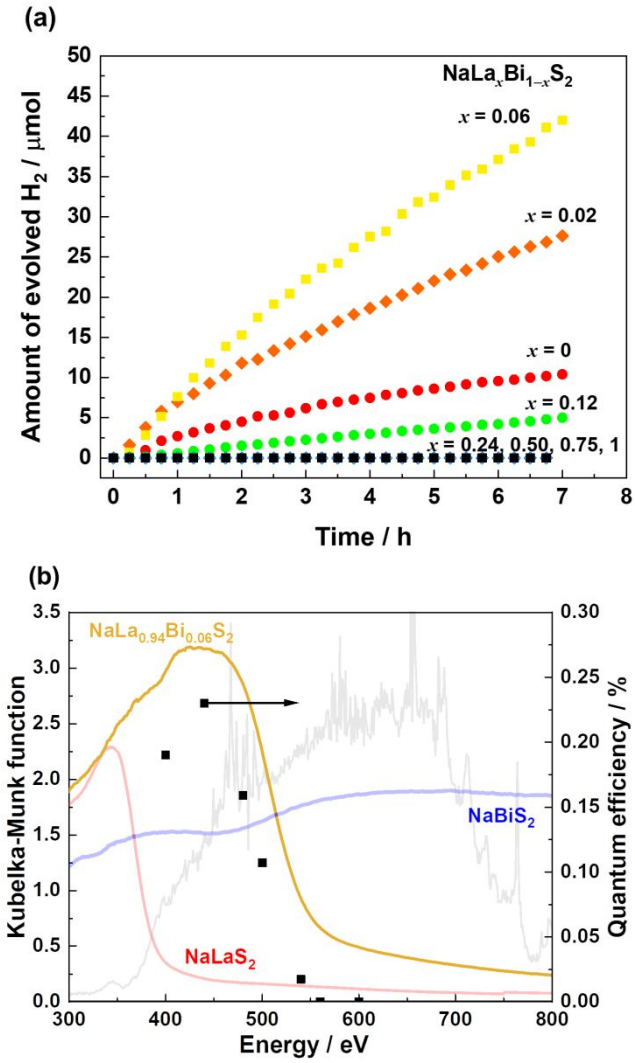

Figure 7. (a) The amount of the evolved H_2 as a function of time using 1 wt% Pt/$NaLa_{1-x}Bi_xS_2$ and (b) action spectra for the $NaLa_{0.94}Bi_{0.06}S_2$ sample together with its Kubelka-Munk function of diffuse reflectance UV-VIS spectra (the spectra for $NaLaS_2$ and $NaBiS_2$ are also shown for reference) as well as the used photon flux in gray (identical data from Figure S2). Conditions: 100 mg photocatalyst, 100 mL of 0.2 M Na_2S, and 0.5 M Na_2SO_3 solution.

The action spectra for the best sample ($NaLa_{0.94}Bi_{0.06}S_2$) are shown in Figure 7b. The photon flux with bandpass filters is demonstrated in Figure S2. The photocatalytic activity nicely matches its absorption spectrum, suggesting that the bandgap excitation was successfully utilized for the photocatalysis. The maximum AQE measured is 0.24% at 420 nm, which needs to be improved for future work. The photocatalytic rates dropped dramatically with a rate less than 1 μmol h^{-1} for $NaLa_{0.88}Bi_{0.12}S_2$ sample (i.e., 12% Bi). All solid solutions had a Bi content of 24% or more and did not generate hydrogen as well as the pristine $NaBiS_2$ although they could effectively harvest visible light according to the UV–Vis DRS results (Figure 3).

One criterion of the photocatalytic activity behavior can be explained by the CBM position whether it is suitable for hydrogen evolution reaction as discussed with the PESA

and UPS data shown in Figure 6. The improved photocatalytic performance of solid solutions with 2% and 6% of Bi ($NaLa_{0.98}Bi_{0.02}S_2$ and $NaLa_{0.94}Bi_{0.06}S_2$) is at least partly attributed to the expansion of the photon absorption range from UV to visible light region as shown in UV–Vis data (Figure 3). There might also be contributions from the exciton dissociation capability associated with the dielectric constant. The drastic decrease in photocatalytic activity for the sample with a Bi substitution greater than 12% is likely due to the fact that the position of these bands relative to the hydrogen evolution potential reduced the electromotive force towards electrocatalytic hydrogen evolution. One way to overcome this problem of the band position would be to tune the particle size, since this geometrical property also affect deeply band positions.[63]

To assess the stability of $NaLaS_2$, $NaLa_{0.98}Bi_{0.02}S_2$, $NaLa_{0.94}Bi_{0.06}S_2$, and $NaLa_{0.88}Bi_{0.12}S_2$ as visible light driven photocatalysts, XRD measurements were performed after 8 h of photocatalysis. The XRD patterns in Figure S14 show identical patterns for all the samples before and after the testing. Under the condition where Na_2S/Na_2SO_3 is present, it is assumed that good stability and robustness of these semiconductors are reasonably achieved during photocatalytic H_2 evolution.

In summary, this study of $NaLa_{1-x}Bi_xS_2$ solid solutions confirms that the optoelectronic properties can be tuned by manipulating the amount of Bi in the structure to be suitable for photocatalytic hydrogen production. The material design concept proposed here might be applicable for selenide and telluride heterostructures materials as isostructures for sulfides. Moreover, $NaLa_{1-x}Bi_xS_2$ with a small bandgap can be utilized as green material for light harvesting applications such as in Z-scheme strategies and solar cell applications.

CONCLUSIONS

The $NaLa_{1-x}Bi_xS_2$ solid solution forms a cubic NaCl type structure confirmed by the Rietveld refinement of XRD patterns and ICP analysis. This provides a monotonic linear shift in lattice constants with their composition. The electronic structure of $NaLa_{1-x}Bi_xS_2$ was measured and computed by DFT calculations using the HSE06 functional. The results show that the Bi *6p* contributes discretely to the CB that occupies the energy level appearing between bands originating from La *5d* and S *3p*. The VBM mainly consists of S *3p* orbitals for the solid solution. Substitution of small Bi contents (up to 6%) in $NaLaS_2$ leads to an extension of the photon absorption from UV of $NaLaS_2$ (3.2 eV) to visible region (2.2 eV). In contrast, all solid solutions with 24% or more Bi content exhibited absorption edges close to that of pure $NaBiS_2$ (1.2 eV). Interestingly, the computed properties show that the $NaBiS_2$ has higher absorption coefficients in the visible region of the spectrum, larger dielectric constants, lower effective masses of charge carriers, and a much lower exciton binding energy than $NaLaS_2$. Thus, good absorption properties and efficient exciton dissociation can be expected in $NaBiS_2$. Experimentally, $NaLa_{1-x}Bi_xS_2$, x~0.06 showed the highest performance of all photocatalytic hydrogen evolution reactions in Na_2S/Na_2SO_3 solution under UV−Vis illumination because of the compensation between enhanced absorption in visible light region and lower electron motive force to achieve hydrogen evolution reaction. The $NaLa_{1-x}Bi_xS_2$ solid solutions are interesting visible light responsive materials for the development of new semiconductors by cation substitution (X^{3+} (ns^2np^0) and Ln^{3+} (ns^0nd^0)) as a tool for bandgap tailoring and band position manipulation.

ASSOCIATED CONTENT

Supporting Information. S1. Experimental protocols; S2. Computational details; S3. Detailed optimization of the synthesis protocol; S4. Characterization; S5. Photocatalytic testing; S6. Supplementary DFT data; S7. Atomic positions provided for PBE0 optimized structures in a POSCAR-like format.

AUTHOR INFORMATION

Corresponding Authors

* Tangui Le Bahers, tangui.le_bahers@ens-lyon.fr;
Kazuhiro Takanabe, takanabe@chemsys.t.u-tokyo.ac.jp

ACKNOWLEDGMENT

Research reported in this work was supported by the King Abdullah University of Science and Technology (KAUST). AB acknowledges Princess Nourah bint Abdulrahman University (PNU) for financial support. NT and TLB acknowledge the PSMN computation center for providing calculation resources.

REFERENCES

1. Sivula, K.; van de Krol, R., Semiconducting Materials for Photoelectrochemical Energy Conversion. *Nat. Rev. Mater.* **2016,** *1*, 15010.

2. Hisatomi, T.; Takanabe, K.; Domen, K., Photocatalytic Water-Splitting Reaction from Catalytic and Kinetic Perspectives. *Catal. Lett.* **2015,** *145*, 95-108.

3. Takanabe, K., Solar Water Splitting Using Semiconductor Photocatalyst Powders. *Top. Curr. Chem.* **2016,** *371*, 73-103.

4. Takata, T.; Pan, C. S.; Domen, K., Recent Progress in Oxynitride Photocatalysts for Visible-Light-Driven Water Splitting. *Sci. Technol. Adv. Mater.* **2015,** *16*, 033506.

5. Ma, G.; Chen, S.; Kuang, Y.; Akiyama, S.; Hisatomi, T.; Nakabayashi, M.; Shibata, N.; Katayama, M.; Minegishi, T.; Domen, K., Visible Light-Driven Z-Scheme Water Splitting Using Oxysulfide H_2 Evolution Photocatalysts. *J. Phys. Chem. Lett.* **2016,** *7*, 3892-3896.

6. Kuriki, R.; Ichibha, T.; Hongo, K.; Lu, D. L.; Maezono, R.; Kageyama, H.; Ishitani, O.; Oka, K.; Maeda, K., A Stable, Narrow-Gap Oxyfluoride Photocatalyst for Visible-Light Hydrogen Evolution and Carbon Dioxide Reduction. *J. Am. Chem. Soc.* **2018,** *140*, 6648-6655.

7. BaQais, A.; Curutchet, A.; Ziani, A.; Ahsaine, H. A.; Sautet, P.; Takanabe, K.; Le Bahers, T., Bismuth Silver Oxysulfide for Photoconversion Applications: Structural and Optoelectronic Properties. *Chem. Mater.* **2017,** *29*, 8679-8689.

8. Pinaud, B. A.; Benck, J. D.; Seitz, L. C.; Forman, A. J.; Chen, Z. B.; Deutsch, T. G.; James, B. D.; Baum, K. N.; Baum, G. N.; Ardo, S.; Wang, H. L.; Miller, E.; Jaramillo, T. F., Technical and Economic Feasibility of Centralized Facilities for Solar Hydrogen Production via Photocatalysis and Photoelectrochemistry. *Energy Environ. Sci.* **2013,** *6*, 1983-2002.

9. Takanabe, K., Photocatalytic Water Splitting: Quantitative Approaches toward Photocatalyst by Design. *ACS Catal.* **2017,** *7*, 8006-8022.

10. Bernechea, M.; Miller, N. C.; Xercavins, G.; So, D.; Stavrinadis, A.; Konstantatos, G., Solution-Processed Solar

Cells Based on Environmentally Friendly $AgBiS_2$ nanocrystals. *Nat. Photonics* **2016,** *10*, 521-525.

11. Gabrel'yan, B. V.; Lavrentiev, A. A.; Nikiforov, I. Y.; Sobolev, V. V., Electronic Energy Structure of $MBiS_2$ (M = Li, Na, K) Calculated with Allowance for the Difference between the M-S and Bi-S Bond Lengths. *J. Struct. Chem.* **2008,** *49*, 788-794.

12. Kang, S.; Hong, Y.; Jeon, Y., A Facile Synthesis and Characterization of Sodium Bismuth Sulfide ($NaBiS_2$) under Hydrothermal Condition. *Bull. Korean Chem. Soc.* **2014,** *35*, 1887-1890.

13. Shockley, W.; Queisser, H. J., Detailed Balance Limit of Efficiency of p-n Junction Solar Cells. *J. Appl. Phys.* **1961,** *32*, 510.

14. Dolgos, M. R.; Paraskos, A. M.; Stoltzfus, M. W.; Yarnell, S. C.; Woodward, P. M., The Electronic Structures of Vanadate Salts: Cation Substitution as a Tool for Band Gap Manipulation. *J. Solid State Chem.* **2009,** *182*, 1964-1971.

15. Fuertes, A., Metal oxynitrides as emerging materials with photocatalytic and electronic properties. *Mater. Horiz.* **2015,** *2*, 453-461.

16. Kishore, M. R. A.; Ravindran, P., Enhanced Photocatalytic Water Splitting in a C_2N Monolayer by C-Site Isoelectronic Substitution. *ChemPhysChem* **2017,** *18*, 1526-1532.

17. Yuan, Y. P.; Lv, J.; Jiang, X. J.; Li, Z. S.; Yu, T.; Zou, Z. G.; Ye, J. H., Large Impact of Strontium Substitution on Photocatalytic Water Splitting Activity of $BaSnO_3$. *Appl. Phys. Lett.* **2007,** *91*, 094107.

18. Barreteau, C.; Berardan, D.; Amzallag, E.; Zhao, L. D.; Dragoe, N., Structural and Electronic Transport Properties in Sr-Doped BiCuSeO. *Chem. Mater.* **2012,** *24*, 3168-3178.

19. Ji, H. S.; Togo, A.; Kaviany, M.; Tanaka, I.; Shim, J. H., Low Phonon Conductivity of Layered BiCuOS, BiCuOSe, and BiCuOTe from First Principles. *Phys. Rev. B* **2016,** *94*, 115203.

20. Nakachi, Y.; Ueda, K., Single crystal growth of LaCuOS by the flux method. *J Cryst Growth* **2008,** *311* (1), 114-117.

21. Ueda, K.; Inoue, S.; Hirose, S.; Kawazoe, H.; Hosono, H., Transparent p-Type Semiconductor: LaCuOS Layered Oxysulfide. *Appl. Phys. Lett.* **2000,** *77*, 2701-2703.

22. Sheets, W. C.; Stampler, E. S.; Kabbour, H.; Bertoni, M. I.; Cario, L.; Mason, T. O.; Marks, T. J.; Poeppelmeier, K. R., Facile Synthesis of BiCuOS by Hydrothermal Methods. *Inorg. Chem.* **2007,** *46*, 10741-10748.

23. Ueda, K.; Hosono, H.; Hamada, N., Energy Band Structure of LaCuOCh (Ch = S, Se and Te) Calculated by the Full-Potential Linearized Augmented Plane-Wave Method. *J. Phys.-Condens. Mat.* **2004,** *16*, 5179-5186.

24. Masuda, H.; Fujino, T.; Sato, N.; Yamada, K., Electrical Properties of Na_2US_3, $NaGdS_2$ and $NaLaS_2$. *Mater. Res. Bull.* **1999,** *34*, 1291-1300.

25. Ohtani, T.; Honjo, H.; Wada, H., Synthesis, Order-Disorder Transition and Magnetic-Properties of $LiLnS_2$, $LiLnSe_2$, $NaLnS_2$ and $NaLnSe_2$ (Ln=Lanthanides). *Mater. Res. Bull.* **1987,** *22*, 829-840.

26. Jarý, V.; Havlák, L.; Bárta, J.; Buryi, M.; Mihóková, E.; Rejman, M.; Laguta, V.; Nikl, M., Optical, Structural and Paramagnetic Properties of Eu-Doped Ternary Sulfides $ALnS_2$ (A= Na, K, Rb; Ln= La, Gd, Lu, Y). *Mater.* **2015,** *8*, 6978-6998.

27. Cotter, J. P.; Fitzmaurice, J. C.; Parkin, I. P., New Routes to Alkali-Metal-Rare-Earth-Metal Sulfides. *J. Mater. Chem.* **1994,** *4*, 1603-1609.

28. Li, H. Y.; Ding, W. Z.; Gu, Z.; Li, H. Q.; Zhao, J. L.; Fu, L., Preparation and Infrared Transmittance of $NaLaS_2$ Ceramics. *Mater. Lett.* **2015,** *156*, 62-64.

29. Isaacs, T. J.; Hopkins, R. H.; Kramer, W. E., Study of $NaLaS_2$ as an Infrared Window Material. *J. Electron. Mater.* **1975,** *4*, 1181-1189.

30. Rosales, B. A.; White, M. A.; Vela, J., Solution-Grown Sodium Bismuth Dichalcogenides: Toward Earth-Abundant, Biocompatible Semiconductors. *J. Am. Chem. Soc.* **2018,** *140*, 3736-3742.

31. Le Bahers, T.; Takanabe, K., Combined theoretical and experimental characterizations of semiconductors for photoelectrocatalytic applications. *J. Photochem. Photobiol. C* **2019**, DOI: 10.1016/j.jphotochemrev.2019.01.001

32. Rodriguezcarvajal, J., Recent Advances in Magnetic-Structure Determination by Neutron Powder Diffraction. *Phys. B* **1993,** *192*, 55-69.

33. Cahen, D.; Kahn, A., Electron Energetics at Surfaces and Interfaces: Concepts and Experiments. *Adv. Mater.* **2003,** *15*, 271-277.

34. Isse, A. A.; Gennaro, A., Absolute Potential of the Standard Hydrogen Electrode and the Problem of Interconversion of Potentials in Different Solvents. *J. Phys. Chem. B* **2010,** *114*, 7894-7899.

35. Qureshi, M.; Takanabe, K., Insights on Measuring and Reporting Heterogeneous Photocatalysis: Efficiency Definitions and Setup Examples. *Chem. Mater.* **2017,** *29*, 158-167.

36. Adamo, C.; Barone, V., Toward Reliable Density Functional Methods without Adjustable Parameters: The PBE0 Model. *J. Chem. Phys.* **1999,** *110*, 6158-6170.

37. Dovesi, R.; Erba, A.; Orlando, R.; Zicovich-Wilson, C. M.; Civalleri, B.; Maschio, L.; Rérat, M.; Casassa, S.; Baima, J.; Salustro, S.; Kirtman, B., Quantum-Mechanical Condensed Matter Simulations with CRYSTAL. *Wiley Interdisciplinary Reviews: Computational Molecular Science* **2018,** *8*, e1360.

38. Kresse, G.; Furthmuller, J., Efficiency of Ab-Initio Total Energy Calculations for Metals and Semiconductors using a Plane-Wave Basis Set. *Comput. Mater. Sci.* **1996,** *6*, 15-50.

39. Le Bahers, T.; Rerat, M.; Sautet, P., Semiconductors Used in Photovoltaic and Photocatalytic Devices: Assessing Fundamental Properties from DFT. *J. Phys. Chem. C* **2014,** *118*, 5997-6008.

40. Madsen, G. K. H.; Singh, D. J., BoltzTraP. A Code for Calculating Band-Structure Dependent Quantities. *Comput. Phys. Commun.* **2006,** *175*, 67-71.

41. Ohkubo, I.; Mori, T., Two-Dimensional Layered Complex Nitrides as a New Class of Thermoelectric Materials. *Chem. Mater.* **2014,** *26*, 2532-2536.

42. Sansone, G.; Ferretti, A.; Maschio, L., Ab Initio Electronic Transport and Thermoelectric Properties of Solids from Full and Range-Separated Hybrid Functionals. *J. Chem. Phys.* **2017,** *147*, 114101.

43. Gajdos, M.; Hummer, K.; Kresse, G.; Furthmuller, J.; Bechstedt, F., Linear Optical Properties in the Projector-Augmented Wave Methodology. *Phys. Rev. B* **2006,** *73*, 045112.

44. Kresse, G.; Hafner, J., Ab Initio Molecular Dynamics for Liquid Metals. *Phys. Rev. B Condens. Mat.* **1993,** *47*, 558-561.

45. Kresse, G.; Hafner, J., Ab-Initio Molecular-Dynamics Simulation of the Liquid-Metal Amorphous-Semiconductor Transition in Germanium. *Phys Rev B* **1994,** *49* (20), 14251-14269.

46. Kresse, G.; Furthmuller, J., Efficient Iterative Schemes for Ab Initio Total-Energy Calculations Using a Plane-Wave Basis Set. *Phys. Rev. B* **1996,** *54*, 11169-11186.

47. Off, M. E., Optical, Structural and Paramagnetic Properties of Eu-Doped Ternary Sulfides $ALnS_2$ (A = Na, K, Rb; Ln = La, Gd, Lu, Y). *Mater.* **2015,** *8*, 6978-6998.

48. Denton, A. R.; Ashcroft, N. W., Vegard's Law. *Phys. Rev. A* **1991,** *43*, 3161-3164.

49. Kasper, E.; Schuh, A.; Bauer, G.; Hollander, B.; Kibbel, H., Test of Vegard's Law in Thin Epitaxial SiGe Layers. *J. Cryst. Growth* **1995,** *157*, 68-72.

50. Boltersdorf, J.; King, N.; Maggard, P. A., Flux-Mediated Crystal Growth of Metal Oxides: Synthetic Tunability of Particle Morphologies, Sizes, and Surface Features for Photocatalysis Research. *CrystEngComm* **2015,** *17*, 2225-2241.

51. Fantauzzi, M.; Elsener, B.; Atzei, D.; Rigoldi, A.; Rossi, A., Exploiting XPS for the Identification of Sulfides and Polysulfides. *RSC Adv.* **2015,** *5*, 75953-75963.

52. Tang, K. B.; An, C. H.; Xie, P. B.; Shen, G. Z.; Qian, Y. T.,

Low-Temperature Synthesis and Characterization of Beta-La_2S_3 Nanorods. *J. Cryst. Growth* **2002,** *245*, 304-308.

53. Cooper, J. K.; Gul, S.; Toma, F. M.; Chen, L.; Liu, Y.-S.; Guo, J.; Ager, J. W.; Yano, J.; Sharp, I. D., Indirect Bandgap and Optical Properties of Monoclinic Bismuth Vanadate. *J. Phys. Chem. C* **2015,** *119*, 2969-2974.

54. Lardhi, S.; Curutchet, A.; Cavallo, L.; Moussab, H.; Le Bahers, T., Ab Initio Assessment of $Bi_{1-x}RE_xCuOS$ (RE = La, Gd, Y, Lu) Solid Solutions as a Semiconductor for Photochemical Water Splitting. *Phys. Chem. Chem. Phys.* **2017,** *19*, 12321-12330.

55. Peter, P. Y.; Cardona, M., *Fundamentals of Semiconductors: Physics and Materials Properties*. Springer-Verlag Berlin Heidelberg: 2010.

56. Le Bahers, T.; Haller, S.; Le Mercier, T.; Barboux P. Assessing the use of BiCuOS for photovoltaic application: from DFT to macroscopic simulation. *J. Phys. Chem. C* **2015**, *119*, 17585-17595.

57. Morbec, J. M.; Galli, G., Charge Transport Properties of Bulk Ta_3N_5 from First Principles. *Phys. Rev. B* **2016,** *93*, 035201.

58. Kudo, A.; Miseki, Y., Heterogeneous Photocatalyst Materials for Water Splitting. *Chem. Soc. Rev.* **2009,** *38*, 253-278.

59. Hisatomi, T.; Kubota, J.; Domen, K., Recent Advances in Semiconductors for Photocatalytic and Photoelectrochemical Water Splitting. *Chem. Soc. Rev*. **2014,** *43*, 7520-7535.

60. Walter, M. G.; Warren, E. L.; McKone, J. R.; Boettcher, S. W.; Mi, Q. X.; Santori, E. A.; Lewis, N. S., Solar Water Splitting Cells. *Chem. Rev.* **2010,** *110*, 6446-6473.

61. Varley, J. B.; Lordi, V., Electrical Properties of Point Defects in CdS and ZnS. *Appl. Phys. Lett.* **2013,** *103*, 102103.

62. Woodbury, H. H., Diffusion of Cd in CdS. *Phys. Rev.* **1964,** *134*, A492.

63. Zhao, J.; Holmes, M. A.; Osterloh, F. E. Quantum confinement controls photocatalysis: a free energy analysis for photocatalytic proton reduction at CdSe nanocrystals. *ACS Nano* **2013**, *7*, 4316-4325.

TOC graphic

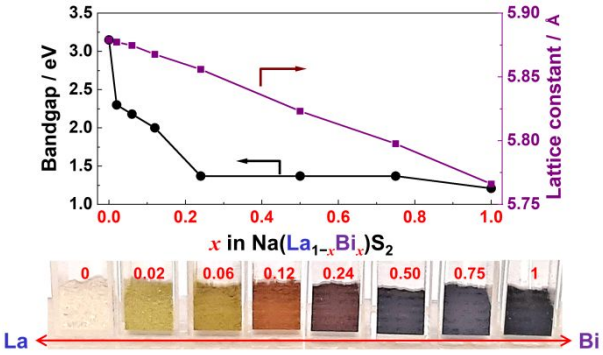
Bandgap / eV
Lattice constant / A
x in Na(La1-xBix)S2
0
0.02
0.06
0.12
0.24
0.50
0.75
1
La
Bi